Manganese Kβ X-ray Emission Spectroscopy As a Probe of Metal–Ligand Interactions

Martha A. Beckwith,[†,‡] Michael Roemelt,[‡,§] Marie-Noëlle Collomb,[‖] Carole DuBoc,[‖] Tsu-Chien Weng,[⊥,○] Uwe Bergmann,[#] Pieter Glatzel,[⊥] Frank Neese,[‡,§] and Serena DeBeer[†,‡,*]

[†]Department of Chemistry and Chemical Biology, Cornell University, Ithaca, New York 14853, United States

[‡]Max-Planck-Institut für Bioanorganische Chemie, Stiftstrasse 34-36, D-45470 Mülheim an der Ruhr, Germany

[§]Institut für Physikalische und Theoretische Chemie, Universität Bonn, D-53115 Bonn, Germany.

[‖]Université Joseph Fourier Grenoble 1/CNRS, Département de Chimie Moléculaire, UMR-5250, Laboratoire de Chimie Inorganique Redox, Institut de Chimie Moléculaire de Grenoble FR-CNRS-2607, BP-53, 38041 Grenoble Cedex 9, France

[⊥]European Synchrotron Radiation Facility, 6 Rue Jules Horowitz, BP 220, Cedex 9, 38043 Grenoble, France

[#]Linac Coherent Light Source, SLAC National Accelerator Laboratory, Menlo Park, California 94025, United States

S *Supporting Information*

ABSTRACT: A systematic series of high-spin mononuclear Mn-(II), Mn(III), and Mn(IV) complexes has been investigated by manganese Kβ X-ray emission spectroscopy (XES). The factors contributing to the Kβ main line and the valence to core region are discussed. The Kβ main lines are dominated by 3p–3d exchange correlation (spin state) effects, shifting to lower energy upon oxidation of Mn(II) to Mn(III) due to the decrease in spin state from $S = 5/2$ to $S = 2$, whereas the valence to core region shows greater sensitivity to the chemical environment surrounding the Mn center. A density functional theory (DFT) approach has been used to calculate the valence to core spectra and assess the contributions to the energies and intensities. The valence spectra are dominated by manganese np to 1s electric dipole-allowed transitions and are particularly sensitive to spin state and ligand identity (reflected primarily in the transition energies) as well as oxidation state and metal–ligand bond lengths (reflected primarily in the transition intensities). The ability to use these methods to distinguish different ligand contributions within a heteroleptic coordination sphere is highlighted. The similarities and differences between the current Mn XES study and previous studies of Fe XES investigations are discussed. These findings serve as an important calibration for future applications to manganese active sites in biological and chemical catalysis.
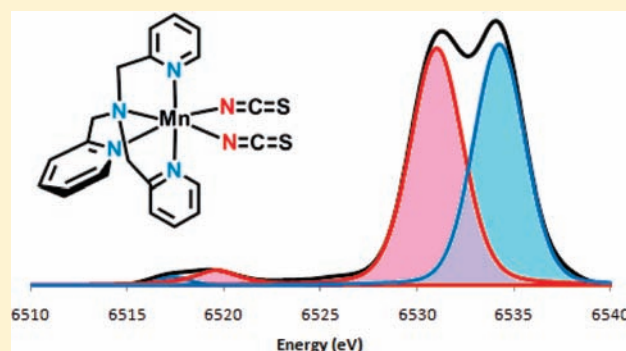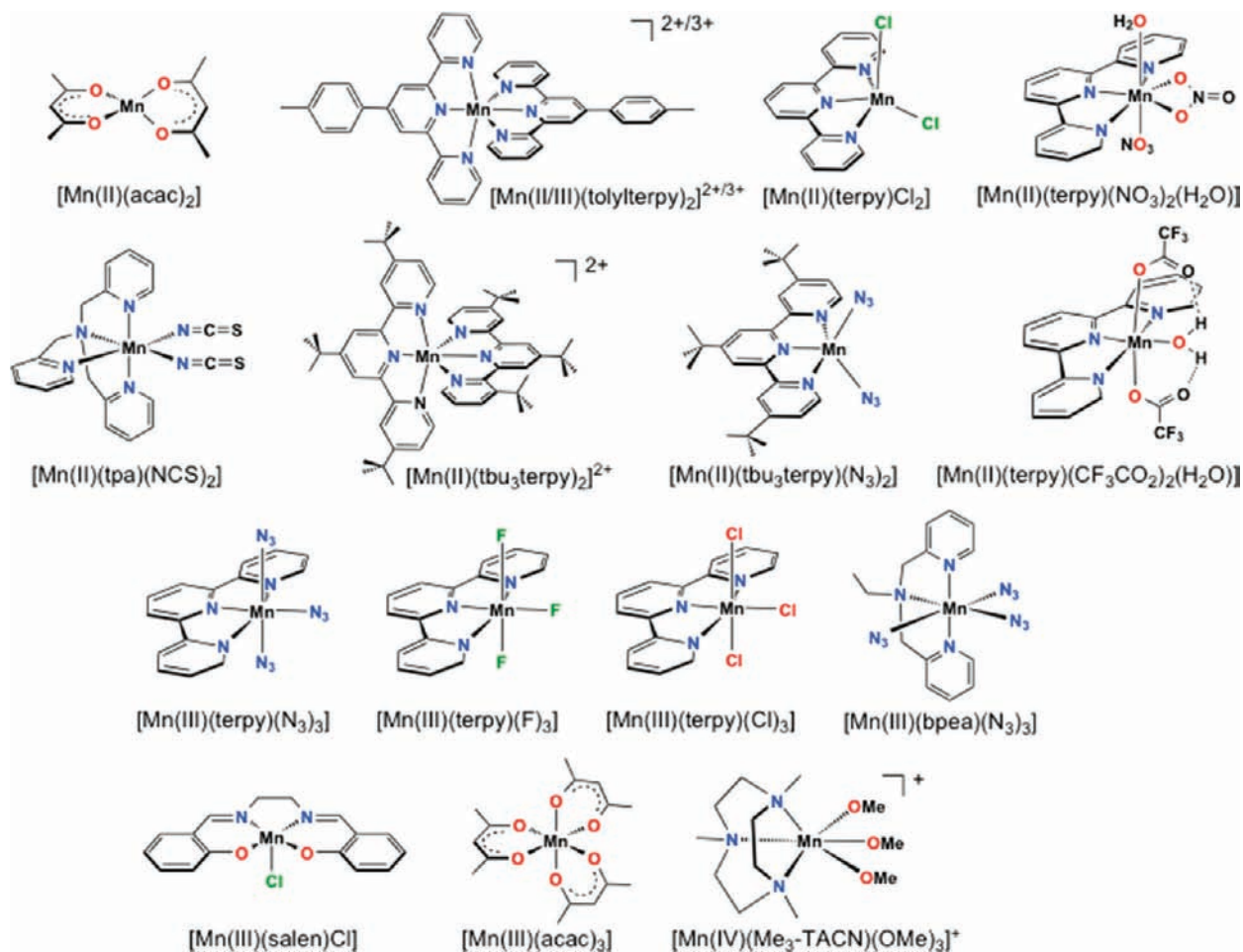
■ INTRODUCTION

Manganese-containing active sites play essential roles in biological and chemical catalysis. Biologically, manganese enzymes are responsible for a wide variety of reactions, ranging from the breakdown of superoxide (by Mn superoxide dismutase)[1–3] to photosynthetic water oxidation (by the Mn_4Ca cluster in Photosystem II).[4,5] In chemical catalysis, small molecule manganese complexes enable a range of oxidative transformations, including alkane hydroxylation and olefin epoxidation.[6–9] In all these reactions, there is fundamental interest in understanding the transformations that occur at the manganese active site and hence an interest in directly probing the Mn electronic structure. EPR spectroscopy has proven to be a powerful tool,[10] particularly in the study of Photosystem II (PSII).[11–13] However, the applicability of EPR to systems with integer ground state spin is limited. This motivates the development of other methods, such as X-ray absorption spectroscopy (XAS). Considerable effort has gone into the application of XAS to Mn systems, as

all oxidation states and spin states of Mn may be probed by X-ray core level spectroscopy.[14–18] For PSII, this has allowed for spectra of the S_0 to S_3 states of the Mn_4Ca cluster to be obtained, thus providing significant insights into the oxidative transformations that occur in the cycle.[19–21] However, despite the advances reported in these studies, questions about the exact nature of some of the S states remain and there is a clear need for additional spectroscopic insights in order to fully assess changes in the electronic structure. In particular, a method that allows one to better assess changes in the ligand environment could provide key insights into our understanding of PSII and would also generally benefit our understanding of biological and chemical catalysis by Mn.

A method that shows potential promise in this regard is Mn Kβ X-ray emission spectroscopy (XES).[22,23] The so-called Mn

Chart 1. Graphical Representation of Manganese Complexes Investigated in This Study[a]

[Mn(II)(acac)₂] · [Mn(II/III)(tolylterpy)₂]²⁺/³⁺ · [Mn(II)(terpy)Cl₂] · [Mn(II)(terpy)(NO₃)₂(H₂O)]

[Mn(II)(tpa)(NCS)₂] · [Mn(II)(tbu₃terpy)₂]²⁺ · [Mn(II)(tbu₃terpy)(N₃)₂] · [Mn(II)(terpy)(CF₃CO₂)₂(H₂O)]

[Mn(III)(terpy)(N₃)₃] · [Mn(III)(terpy)(F)₃] · [Mn(III)(terpy)(Cl)₃] · [Mn(III)(bpea)(N₃)₃]

[Mn(III)(salen)Cl] · [Mn(III)(acac)₃] · [Mn(IV)(Me₃-TACN)(OMe)₃]⁺

[a] A complete list of complexes is given in Table 1.

$K\beta$ main line corresponds to a dipole-allowed Mn 3p–1s transition, which exhibits pronounced sensitivity to spin state.[11,24–26] To higher energy is the valence to core region, which corresponds to transitions from valence orbitals into the Mn 1s core hole.[27,28] Recently, systematic studies of Fe $K\beta$ XES spectra have shown that the intensity of the valence to core features are mediated by Fe np mixing into the filled ligand orbitals.[29] The resultant spectra have a pronounced sensitivity to metal spin state, oxidation state, and identity of the bound ligand (including ionization state, protonation state, and hybridization).[29] Smolentsev et al. carried out a limited subset of studies on Mn complexes,[30] which show parallel trends to the iron study. However, to our knowledge, a detailed, systematic investigation of Mn complexes with varied oxidation states and ligand environments has not yet been reported in the literature. These studies are of particular interest as Mn $K\beta$ XES valence to core data are already available for the S_1 state of the Mn₄Ca cluster in PSII.[31] The data show that the S_1 state has several μ-oxo-bridged Mn–O bonds; however, at this stage only an empirical assessment of the data can be made. A more quantitative analysis of the data requires a systematic study of a range of compounds and correlation of these data to theory.

Here, we present a systematic study of the $K\beta$ XES spectra of 16 high-spin mononuclear Mn(II), Mn(III), and Mn(IV) complexes

(Chart 1 and Table 1). The oxidation and spin state contributions to both the $K\beta$ main line and the valence to core region are assessed. While the spin state dependence of the $K\beta$ main line has been previously investigated, to our knowledge, the spin state contribution to the valence to core region has not been examined in detail. In addition, the contributions of oxidation state and ligand identity to the valence to core region are investigated and quantitatively evaluated.

The experimental valence to core transitions are compared to those calculated using a straightforward density functional theory (DFT) approach, as previously applied in Fe XES studies.[29] The strong correlation between experiment and theory indicates that these calculated spectra can be used for a quantitative analysis of valence orbital composition. This also allows the contributions of spin state, ligand identity, and metal–ligand bond lengths to be assessed in an in silico fashion. The potential of these methods for probing questions in biological manganese catalysis is highlighted.

■ EXPERIMENTAL SECTION

Sample Preparation. [Mn(II)(acac)₂], [Mn(III)(acac)₃], and [Mn(III)salenCl] were purchased from Strem Chemicals and used without further purification. All other manganese reference samples

Table 1. $K\beta_{1,3}$ Peak Energies, $K\beta_{2,5}$ Intensity-Weighted Average Energies, and Background-Subtracted Valence to Core Areas of the Mn Model Complexes Studied

complex	$K\beta_{1,3}$ energy (eV)[a]	$K\beta_{2,5}$ energy (eV)[b]	area (valence to core region)[c]	ref[d]
		Mn(II) complexes		
$[Mn(acac)_2]$	6491.85	6531.9 (0.01)	12.02 (0.41)	
$[Mn(tolylterpy)_2]^{2+}$	6491.89	6533.04 (0.05)	16.12 (0.12)	42,43
$[Mn(terpy)Cl_2]$	6491.83	6533.45 (0.02)	11.37 (0.09)	36
$[Mn(terpy)(NO_3)_2(H_2O)]$	6492.04	6532.47 (0.17)	13.20 (0.52)	32
$[Mn(tbu_3terpy)_2]^{2+}$	6491.87	6532.82 (0.09)	14.71 (0.64)	34
$[Mn(tbu_3terpy)(N_3)_2]$	6491.6	6532.31 (0.10)	18.36 (0.11)	39
$[Mn(terpy)(CF_3CO_2)_2(H_2O)]$	6492.03	6532.85 (0.01)	14.37 (0.13)	41
$[Mn(tpa)(NCS)_2]$	6491.76	6532.68 (0.01)	13.91 (0.16)	34
		Mn(III) complexes		
$[Mn(acac)_3]$	6491.53	6531.62 (0.13)	17.47 (1.06)	
$[Mn(tolylterpy)_2]^{3+}$	6491.48	6532.83 (0.01)	25.90 (0.31)	43
$[Mn(terpy)(N_3)_3]$	6491.42	6532.09 (0.01)	21.52 (0.18)	35
$[Mn(terpy)F_3]$	6491.71	6532.85 (0.04)	19.03 (0.75)	38
$[Mn(terpy)Cl_3]$	6491.63	6533.19 (0.15)	17.10 (0.55)	37
$[Mn(bpea)(N_3)_3]$	6491.43	6532.35 (0.01)	18.91 (0.04)	38
$[Mn(salen)Cl]$	6491.25	6532.15 (0.05)	21.01 (0.70)	
		Mn(IV) complexes		
$[Mn(Me_3\text{-}TACN)(OMe)_3]^+$	6491.25	6532.78 (0.04)	20.06 (0.70)	33,40

[a] Estimated error in the $K\beta_{1,3}$ energy is ± 0.1 eV. [b] Intensity-weighted average energies were determined using the $K\beta_{2,5}$ region (6525–6540 eV). Satellite features in the <6525 eV range are not included in the reported areas as these are generally poorly resolved from the background and thus have larger errors associated with determination of the areas. Standard deviations for the energy and area of each complex are given in parentheses. The reported values for the energies and areas are those obtained from the best fit, with the standard deviations based on all reasonable fits reported in parentheses. [c] Reported areas are out of 1000 units of normalized intensity. [d] Synthesis and crystallographic structure references.

were synthesized according to published procedures.[32−43] The references for the syntheses and the crystal structures are provided in Table 1. The following abbreviations have been used for the ligands: acac = acetyl acetonate; bpea = N,N-bis(2-pyridylmethyl)ethylamine; Me₃-TACN = 1,4,7-trimethyl-1,4,7-triazacyclononane; salen = ethylenebis(salicylimine); tbu₃terpy = 4,4′,4″-tri-*tert*-butyl-2,2′:6′,2″-terpyridine; terpy = 2,2′:6′,2″-terpyridine; tolylterpy = 4′-(4-methylphenyl)-2,2′:6′,2″-terpyridine; tpa = tris-2-picolylamine (see also Chart 1). Samples were measured as powders, diluted in boron nitride, pressed into pellets, and sealed into Al spacers with 38 μm Kapton tape. All samples were loaded into a liquid helium cryostat and maintained at a temperature of ∼20 K throughout the course of data collection.

XES Measurements. All XES data were obtained at beamline ID26 of the European Synchrotron Radiation Facility (ESRF). A pair of Si crystals in 311 reflection was used upstream for energy selection and fixed at an incident energy of 6700 eV. The incident flux was 10^{13} photons/second in a 0.2×1.5 mm² beam footprint on the sample. $K\beta$ X-ray emission spectra were measured using the 440 reflection of five spherically bent ($R = 1$ m) Si crystal analyzers in combination with a silicon drift detector aligned in a Rowland geometry, as described previously.[30] The overall energy bandwidth of the X-ray emission spectrometer was 0.8 eV. The data were normalized with respect to the incident flux. The space between the sample, the spherical analyzers, and the detector was filled with helium in order to minimize attenuation of the fluorescence. In order to assess the rate of photoreduction, short $K\beta$ detected XANES scans were run to determine the acceptable dwell time per sample spot. For all samples data were obtained on multiple spots. Only those scans which showed no evidence for photoreduction were included in the final averages. Both short and long scans of the XES data were obtained. The long scans included both the $K\beta$ main line (6478−6550 eV) and the valence

to core region, whereas the short scans (6505−6550 eV) included only the valence to core region.

The experimental spectra were obtained by first separately averaging long scans and short scans in PyMCA[44] and then merging the resultant average scans together to obtain the full spectra. For each of the averaged spectra, the total integrated area was set to a value of 1000 and the valence to core region was fit using the program EDG_FIT.[45] The background tail from the $K\beta$ main line and the valence to core features were modeled using a combination of Gaussian and Lorenztian functions. The background from the $K\beta$ main line was subtracted from the reported valence to core areas. The reported areas represent the best fit based on minimized error, with the standard deviations of all reasonable fits reported in parentheses (Table 1).

XES Calculations. All calculations have been carried out with ORCA quantum chemistry program package using the methods developed in ref 29. Geometry optimizations were performed starting from X-ray crystal structures (when available and as referenced in Table 1). The BP86 functional,[46,47] the zeroth order regular approximation for relativistic effects (ZORA)[48] following the model potential implementation of van Wüllen,[49] and the scalar-relativistically recontructed def2-TZVP(-f) basis set were used in all of these calculations.[50] Solvation effects were accounted for by the conductor-like screening model (COSMO)[51] using the dielectric constant of dichloromethane ($\varepsilon = 9.08$). A dense grid (ORCA Grid4) was used for the numerical integration of the exchange-correlation potential.

All Mn K-edge XES calculations presented in this study have been conducted using the theoretical protocol described above. In contrast to the previously described method for calculating XES spectra,[29] the molecular orbitals used were corrected for spin−orbit coupling (SOC). The calculated XES spectra using SOC are similar to those without SOC in the region of interest for the complexes studied. The SOC operator is

approximated by the spin−orbit mean-field method (SOMF)[52] where it appears as an effective one-electron operator

$$\hat{H}^{SOMF} = \sum_i \hat{\mathbf{h}}^{SOC}(i)\hat{\mathbf{s}}(i) \tag{1}$$

The summation is over all electrons i. Spin−orbit-corrected orbitals are then obtained by diagonalizing the SOC operator in the basis of the already converged scalar-relativistic Kohn−Sham orbitals. The sum of the Kohn−Sham and the SOC operator thus takes the form

$$\left(\left(\begin{pmatrix} \varepsilon^\alpha & \\ & \varepsilon^\beta \end{pmatrix} + \frac{1}{2}\begin{pmatrix} \mathbf{h}_z^{SOC} & \mathbf{h}_x^{SOC} + i\mathbf{h}_x^{SOC} \\ \mathbf{h}_x^{SOC} - i\mathbf{h}_x^{SOC} & -\mathbf{h}_z^{SOC} \end{pmatrix}\right)\right)\begin{pmatrix} \mathbf{V}_\alpha \\ \mathbf{V}_\beta \end{pmatrix}$$
$$= \varepsilon_p \begin{pmatrix} \mathbf{V}_\alpha \\ \mathbf{V}_\beta \end{pmatrix} \tag{2}$$

Here, $\mathbf{h}_\mu^{SOC}$ ($\mu = x, y, z$) denotes the Cartesian components of the effective one-electron SOMF operator and ε^α and ε^β are diagonal matrices that contain the scalar relativistic orbital energies as diagonal elements. The diagonalization procedure yields SOC-corrected orbital energies ε_p and orbitals that are linear combinations of the spin-free molecular spin orbitals

$$|p\rangle = \sum_{r_\alpha} V_{r_\alpha p}|r_\alpha\rangle + \sum_{r_\beta} V_{r_\beta p}|r_\beta\rangle \tag{3}$$

Transition moments (electric dipole, magnetic dipole, and electric quadrupole) between these orbitals are calculated using

$$\langle p|\hat{\mathbf{m}}|q\rangle = \sum_{r_\alpha, s_\alpha} V^*_{r_\alpha p} V_{s_\alpha q}\langle r_\alpha|\hat{\mathbf{m}}|s_\alpha\rangle$$
$$+ \sum_{r_\beta, s_\beta} V^*_{r_\beta p} V_{s_\beta q}\langle r_\beta|\hat{\mathbf{m}}|s_\beta\rangle \tag{4}$$

Here, p and q are two SOC-corrected (complex) orbitals and r and s sum over the original spin orbitals. Note that the coefficient matrices V are complex, and hence, the complex conjugate coefficients $V^*_{r_\alpha p}$ and $V^*_{r_\beta p}$ occur in eq 4.

■ RESULTS AND DISCUSSION

Kβ XES Main Line Spectra. Mn Kβ emission data were obtained for a series of high-spin mononuclear Mn(II) and Mn(III) complexes in addition to one Mn(IV) complex, as summarized in Table 1. The Kβ main line corresponds to a Mn 3p to 1s transition. Its energy should be affected by contributions from both 3p−3d exchange, variations in the effective nuclear charge (Z_{eff}) of the manganese centers, and perhaps also smaller contributions from SOC arising from the $3p^5$ final state configuration. The Kβ main line spectra for the complexes investigated in this study are given in the Supporting Information (Figures S1A−S1D). The energy positions of the intensity maxima of the $K\beta_{1,3}$ features are given in Table 1.

The Kβ' feature, which appears on the low-energy side of the Kβ main line, could not be obtained due to constraints on the geometry imposed by the cryostat windows. As this region is not the primary focus of the current study, truncation of the data range does not significantly impact the reported data. However, we note that the absence of the Kβ' feature may result in a slightly larger error in the normalized valence to core areas (vide infra). We also note that even in the absence of the Kβ' feature, interesting trends may be observed in the $K\beta_{1,3}$ main line energies. As shown in Table 1, the $K\beta_{1,3}$ main line shifts to slightly lower energy upon oxidation of Mn(II) to Mn(III). This is most clearly illustrated by comparing the data of [Mn(II)-(tolylterpy)$_2$]$^{2+}$ to that of [Mn(III)(tolylterpy)$_2$]$^{3+}$, which have

Kβ main line energies of 6491.9 and 6491.5 eV, respectively. This 0.4 eV decrease in energy is the result of two primary contributions: (1) the change in Z_{eff} upon oxidation (which should tend to *increase* the energy of the $K\beta_{1,3}$ main line, due to a greater stabilization of the Mn 1s orbital relative to the Mn 3p orbitals) and (2) the change in spin state from $S = 5/2$ for Mn(II) to $S = 2$ for Mn(III) (which will tend to *decrease* the 3d−3p exchange splitting, thus decreasing the $K\beta':K\beta_{1,3}$ splitting and lowering the energy of the main line feature). The observed overall decrease in energy indicates that the exchange splitting is the larger contributor in these compounds, a trend generally observed for high-spin Mn systems.

This observation is different from what has been observed for Fe Kβ emission data, where the $K\beta_{1,3}$ feature shifts to *higher* energy (by ∼0.8 eV) upon oxidation of Fe(II) to Fe(III). This is correlated to the fact that for high-spin Fe(II) oxidation results in an increase in spin state from $S = 2$ to $S = 5/2$. Thus, for a high-spin Fe(II)/Fe(III) redox couple the Kβ main lines spin state and Z_{eff} effects have an additive effect upon oxidation, resulting in a larger overall increase in the Kβ main line energy, whereas for a high-spin Mn(II)/Mn(III) redox couple these effects oppose each other. On the basis of these observations, one can *roughly* estimate the increased 3p−3d exchange contribution resulting from increasing the Mn spin state by one electron. Assuming that the contributions for an increase in Z_{eff} by one oxidation state are approximately equal for Fe and Mn, then a ∼0.2 eV increase in the Kβ main line energy to the Z_{eff} change at the metal is obtained. This then indicates a ∼0.6 eV change due to an increase in spin state by one-half unit of spin angular momentum brought about by an additional unpaired electron. This is reasonably consistent with the ∼2 eV increase in energy observed on going from low-spin ferrous or ferric complexes to the corresponding high-spin complexes (i.e., an increase of 4 in multiplicity). We note that these values are simply rough estimates to explain observed experimental trends in closely related molecular complexes and additional factors, such as metal−ligand covalency, may also play a role.[53] However, the general trends indicate that the energies of Kβ main lines provide useful markers for changes in the spin state of a system, as also indicated previously.[23] More detailed analyses of the $K\beta_{1,3}$ main line features are ongoing in our laboratory.

Kβ XES Valence to Core Spectra. Figure 1A,B and 1 C,D presents the valence to core spectra for the Mn(II) and Mn(III) complexes, respectively, investigated in this study. Table 1 reports the intensity-weighted average energies for the Mn XES valence to core spectra and the corresponding areas.

Valence to Core Energies. Upon oxidation of Mn(II) to Mn(III), there is a slight shift to lower energy when comparing complexes with identical ligands (Table 1). For example, on going from [Mn(II)(tolylterpy)$_2$]$^{2+}$ to [Mn(III)(tolylterpy)$_2$]$^{3+}$ the valence to core region of the spectra shifts down in energy by 0.2 eV. This shift is smaller than the shift in the Mn Kβ main line (∼0.4 eV) for the same set of complexes and may reflect a slightly larger contribution from the change in Z_{eff} to the valence to core energies. The shift for the Mn complexes is again significantly smaller than what has been observed for Fe complexes, where an ∼1.2 eV increase in energy is observed upon oxidation. We note that the energy of the mononuclear Mn(IV) complex, [Mn(IV)(Me$_3$-TACN)(OMe)$_3$]$^+$, falls within the range of the Mn(III) complexes; however, without a comparison to a complex in an analogous ligation sphere, a more quantitative assessment is not possible.
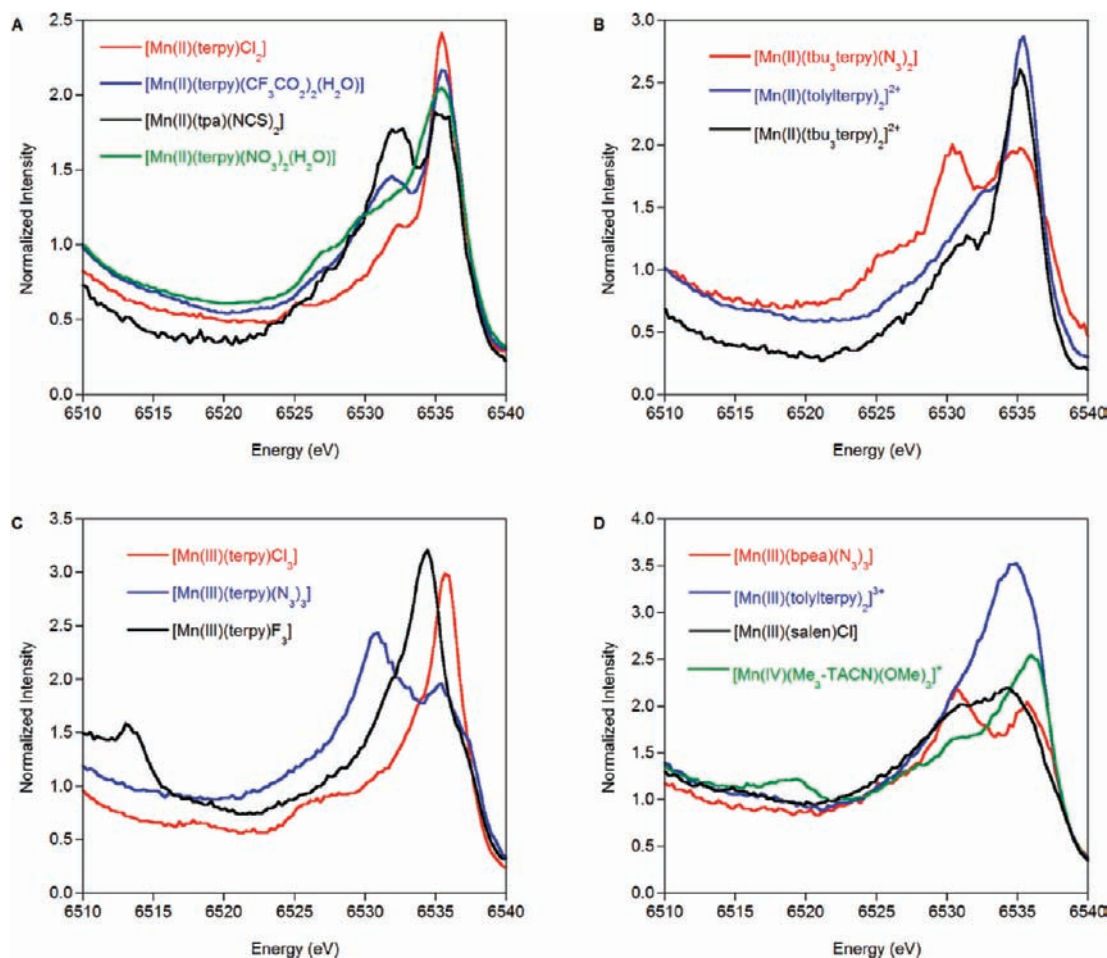
Figure 1. (A and B) Valence to core region for Mn(II) complexes. (C and D) Valence to core region for Mn(III) complexes.

Valence to Core Areas. The experimental areas for the valence to core region span ~11−18 units of intensity for the Mn(II) complexes and increase to 17−26 units of intensity for the Mn(III) complexes. When comparing $[Mn(II)(tolylterpy)_2]^{2+}$ to $[Mn(III)(tolylterpy)_2]^{3+}$, an increase in intensity by a factor of 1.6 is observed upon oxidation. This is attributed to the shorter Mn−ligand bond lengths which provide a mechanism for increased Mn np mixing into the ligand orbitals.[29]

We note, however, that $[Mn(IV)(Me_3\text{-}TACN)(OMe)_3]^+$ does not show the most intense peaks in this region despite having the highest oxidation state. This likely reflects the relatively long average Mn(IV)−ligand bond lengths for this complex, which fall within the range of the Mn(III) complexes, thus resulting in comparable peak intensities.

It is again of interest to note that this is in contrast to our previous observations for Fe valence to core XES spectra, where high-spin ferrous and ferric complexes exhibited similar areas, with only a ~10% increase in intensity upon oxidation. This in part reflects the more substantial structural change on going from Mn(II) to Mn(III), as the latter is subject to a large Jahn−Teller distortion.

Valence to Core Spectral Features. In addition to the changes in the areas and energies, the valence to core region also shows pronounced changes in the number and distribution of spectral features. This is in contrast to the $K\beta_{1,3}$ main line spectra (Figure S1, Supporting Information) which are very similar and

highlights the sensitivity of the valence to core spectra to the chemical environment. Note that due to the richly featured nature of the $K\beta_{2,5}$ region, it is difficult to pick a single peak maximum, and therefore, the intensity-weighted average energy of the $K\beta_{2,5}$ features (6525−6540 eV) is reported (Table 1). For the Mn(III) series, $[Mn(III)(terpy)F_3]$, $[Mn(III)(terpy)Cl_3]$, and $[Mn(III)(terpy)(N_3)_3]$ shown in Figure 1C, the energies of both the more intense $K\beta_{2,5}$ features (~6525−6540 eV) and the satellites (~6510−6525 eV) reflect the differences in ionization energies of the bound ligands. It is also interesting to note that there are two intense features in the spectrum of $[Mn(III)(terpy)(N_3)_3]$ (at 6530 and 6535 eV), possibly reflecting differences between the coordination of the nitrogen atoms from the terpy and the azide ligands. Similar trends are observed for the spectra shown in Figure 1D, with the spectrum of $[Mn(III)(bpea)(N_3)_3]$ showing a similar intense bimodal feature to higher energy.

There are also subtle differences in the spectra of the two Mn(II) complexes $[Mn(II)(tbu_3terpy)_2]^{2+}$ and $[Mn(II)(tolylterpy)_2]^{2+}$ (Figure 1B), despite the fact that in both complexes the atoms directly bound to the metal are all terpy nitrogens. This suggests that the overall nature of the ligand affects the observed spectral features. The spectra of $[Mn(II)(tbu_3terpy)(N_3)_2]$ and $[Mn(II)\text{-}(tpa)(NCS)_2]$ both show the intense bimodal feature similar to $[Mn(III)(terpy)(N_3)_3]$. These spectra are in contrast to the homoleptic spectra for $[Mn(II)(tbu_3terpy)_2]^{2+}$ and

Table 2. K$\beta_{2,5}$ Intensity-Weighted Average Energies and Valence to Core Areas for the Calculated Spectra of the Mn Model Complexes Studied[a]

complex	K$\beta_{2,5}$ intensity-weighted average energy (eV)[b]	transition moment	predicted experimental area[c]
Mn(II) complexes			
[Mn(acac)$_2$]	6531.98	8.50×10^{-3}	12.89
[Mn(tolylterpy)$_2$]$^{2+}$	6532.34	8.44×10^{-3}	14.52
[Mn(terpy)Cl$_2$]	6533.12	7.93×10^{-3}	14.26
[Mn(terpy)(NO$_3$)$_2$(H$_2$O)]	6532.02	7.13×10^{-3}	12.20
[Mn(tbu$_3$terpy)$_2$]$^{2+}$	6532.29	8.49×10^{-3}	14.53
[Mn(tbu$_3$terpy)(N$_3$)$_2$]	6531.75	9.83×10^{-3}	16.84
[Mn(terpy)(CF$_3$CO$_2$)$_2$(H$_2$O)]	6531.85	7.42×10^{-3}	12.85
[Mn(tpa)(NCS)$_2$]	6531.71	8.56×10^{-3}	14.54
Mn(III) complexes			
[Mn(acac)$_3$]	6532.2	1.16×10^{-2}	22.51
[Mn(tolylterpy)$_2$]$^{3+}$	6533.24	1.31×10^{-2}	23.75
[Mn(terpy)(N$_3$)$_3$]	6532.21	1.27×10^{-2}	22.22
[Mn(terpy)F$_3$]	6533.15	1.15×10^{-2}	24.70
[Mn(terpy)Cl$_3$]	6534.01	1.00×10^{-2}	18.96
[Mn(bpea)(N$_3$)$_3$]	6532.3	1.21×10^{-2}	21.24
[Mn(salen)Cl]	6532.96	1.55×10^{-2}	30.06
Mn(IV) complexes			
[Mn(Me$_3$-TACN)(OMe)$_3$]$^+$	6533.07	1.55×10^{-2}	30.97

[a] The theoretical transition moments include the electric dipole, electric quadrupole, and magnetic dipole contributions. [b] Intensity-weighted average energies determined using the K$\beta_{2,5}$ peaks (6525–6540 eV). Satellite features in the <6525 eV range are not included in the reported areas. A 59.2 eV energy shift has been applied to all calculated energies. [c] Predicted experimental areas determined using the calculated areas and an area correlation fit line, $y = (5.73 \times 10^{-4})x + 6.79 \times 10^{-4}$.

[Mn(II)(tolylterpy)$_2$]$^{2+}$ and suggest that the valence to core spectra may allow for separation of different ligand contributions within heteroleptic environments.

Calculation of Valence to Core XES Spectra. In order to better understand the observed trends in the experimental data, DFT calculations were used to model the valence to core regions of the XES spectra. As noted above, the reported experimental energies (Table 1) correspond to the intensity-weighted average energy of the K$\beta_{2,5}$ features (6525–6540 eV) in the valence to core region. Analogous intensity-weighted average energies were obtained for the calculated data by first applying a constant energy shift and then weighting the calculated intensity over the same region. Only the K$\beta_{2,5}$ feature was used to calculate the valence to core intensity-weighted average energies due to the strong background from the Kβ main line in the experimental spectra, which in many cases obscures the satellite features. Table 2 shows the calculated valence to core energies and the areas for the calculated spectra. For consistency, the same averaging procedure that was used for the experimental data has also been applied to the theoretical results.

Analogous calculations were not used to predict the Kβ main lines because it was previously found that DFT underestimates the core-level spin polarization and therefore also strongly underestimates the 3p–3d exchange splitting.[54] In addition, the relative intensity ratios between the Kβ' and the K$\beta_{1,3}$
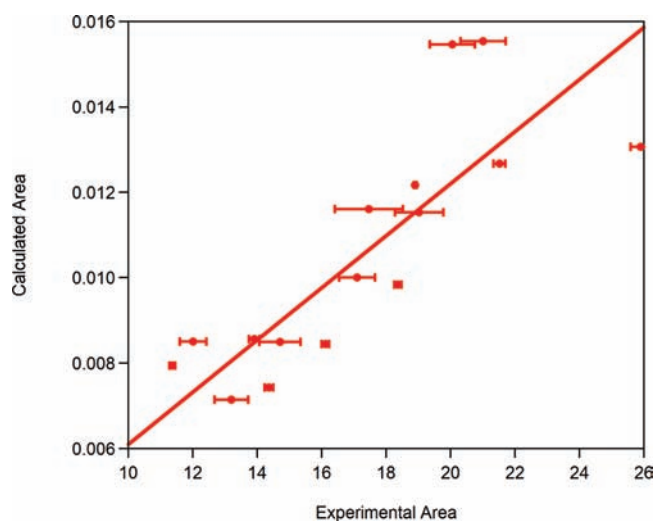

Figure 2. Calculated vs experimental valence to core areas. The line has been forced through the origin and gives a slope of $6.10 \times 10^{-4} \pm 8.97 \times 10^{-5}$ units of intensity/calculated fosc. Error bars represent one standard deviation.

features cannot be accurately reproduced within a one-electron DFT picture due to the multiconfigurational nature of these transitions. Thus, refined methods are needed in order to theoretically assess this region of the spectra. Progress has been made using multiplet calculations, though we note a considerable number of empirical parameters are required to simulate the spectra using such an approach and thus limits the predictive capability.[23,55] In contrast, for the valence to core transitions there usually is a very good correlation between the calculated and the experimental spectral shapes. However, we note in some cases that peaks are present in the experimental spectra that cannot be modeled by the simple one-electron picture used in the calculations. These features will be discussed separately below.

The calculated energies are underestimated for all of the complexes studied here. Using the Mn(II), Mn(III), and Mn(IV) complexes as calibrations, an average energy shift of ~59.2 ± 0.6 eV was required to align theory with experiment. The necessity of applying a constant shift that is specific for each density functional and basis set combination but independent of the nature of the chemical species has been discussed at length before and is analogous for XAS and XES calculations.[29,56,57]

Using only the Mn(II) complexes, the energy shift is ~59.7 ± 0.3 eV, while using only the Mn(III) complexes the energy shift is ~58.7 ± 0.3 eV. Hence, the calculated spectra show a shift to slightly higher energy upon oxidation of Mn(II) to Mn(III), which is in contrast to what was observed experimentally. It may be speculated that this results from the underestimated core-level spin polarization that is intrinsic to pure DFT functionals, which incompletely cancels the contributions to the variations brought about by the changes in the effective nuclear charge of the manganese center (vide supra). However, we refrain from introducing oxidation state specific shifts and hence tolerate a slightly larger error obtained by averaging the shift over all oxidation states.

The relationship between the calculated and the experimental areas is shown in Figure 2. The calculated area is proportional to the calculated oscillator strength, which is composed of electric dipole, electric quadrupole, and magnetic dipole contributions. Closer inspection reveals that, as expected, the oscillator strength is dominated by electric dipole transitions (~96% on average).

8402

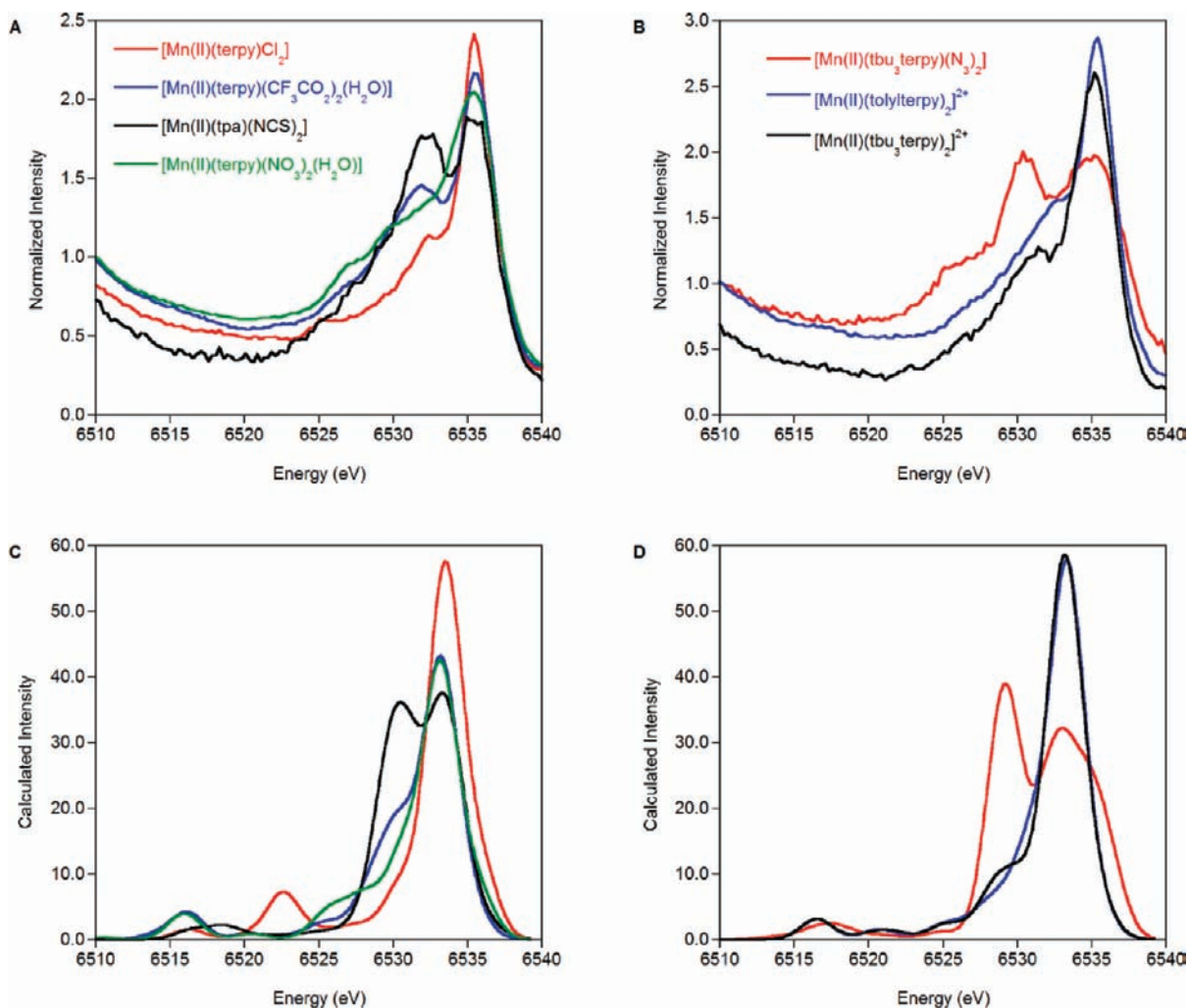dx.doi.org/10.1021/ic200970t |*Inorg. Chem.* 2011, 50, 8397–8409

Figure 3. (A and B) Experimental valence to core region for Mn(II) complexes. (C and D) Corresponding calculated spectra. A constant shift of 59.2 eV and a 2.5 eV broadening have been applied to all calculated spectra.

The relationship between the experimental and the calculated areas for the valence to core region was found to be fairly linear, with a slope of $6.10 \times 10^{-4} \pm 8.97 \times 10^{-5}$ units of intensity/calculated fosc. We also note that the calculation faithfully reproduces the trend in experimental areas, with the Mn(II) complexes having smaller areas and the Mn(III) areas increasing.

With a reasonably linear correlation established between the calculated and experimental energies and intensities, it is interesting to compare the experimental and theoretical spectra more closely. Figures 3 and 4 show the comparisons between the experimental valence to core spectra in Figure 1 to their respective calculated spectra. A constant shift of 59.2 eV and a broadening of 2.5 eV have been applied to all of the calculated spectra. These comparisons demonstrate that the calculations reasonably predict the spectral shapes in terms of relative splittings and intensity distributions of observed valence to core features.

We note that in some cases features calculated in the 6510−6525 eV satellite region are very weak or even absent in the experimental spectra, whereas in other cases satellite features with similar calculated intensities are clearly observed. This is most easily seen when comparing the experimental and calculated spectra of $[\text{Mn(III)(terpy)Cl}_3]$ and $[\text{Mn(III)(terpy)(N}_3)_3]$ in Figure 4A and 4C, respectively. For $[\text{Mn(III)(terpy)Cl}_3]$ even

the very weak feature at ∼6518 eV (with ∼4 units of calculated intensity) is observed experimentally, while for $[\text{Mn(III)(terpy)-}$ $(\text{N}_3)_3]$ the calculated feature at 6518 eV (with ∼8 units of intensity) is not observed. This may in part be attributed to variations in the strong background from the Kβ main line, which may obscure weaker features in the experimental spectra. These observations provide insight into an intensity threshold that is needed in the calculated spectra in order for satellite features to be clearly seen above the background in the experiment. Assuming similar background contributions from the Kβ main line, as with the spectra in Figure 4B, it is conservatively estimated that at least ∼15−20 calculated intensity units are needed in order for a calculated satellite feature to be observed experimentally. This estimate will change, of course, with varying degrees of background intensity but represents a helpful rule of thumb when one is aiming at using the calculated spectra in a predictive fashion.

Nature of the Valence to Core Features. *[Mn(III)(terpy)Cl₃].* As mentioned previously, the valence to core spectra are dominated by dipole-allowed Mn np to Mn 1s transitions. Within the chosen approach, the calculated XES spectra exclusively reflect the single-particle spectrum of the system under investigation. Thus, all features can be interpreted in terms of molecular orbitals rather than many electron states. This greatly simplifies the discussion,
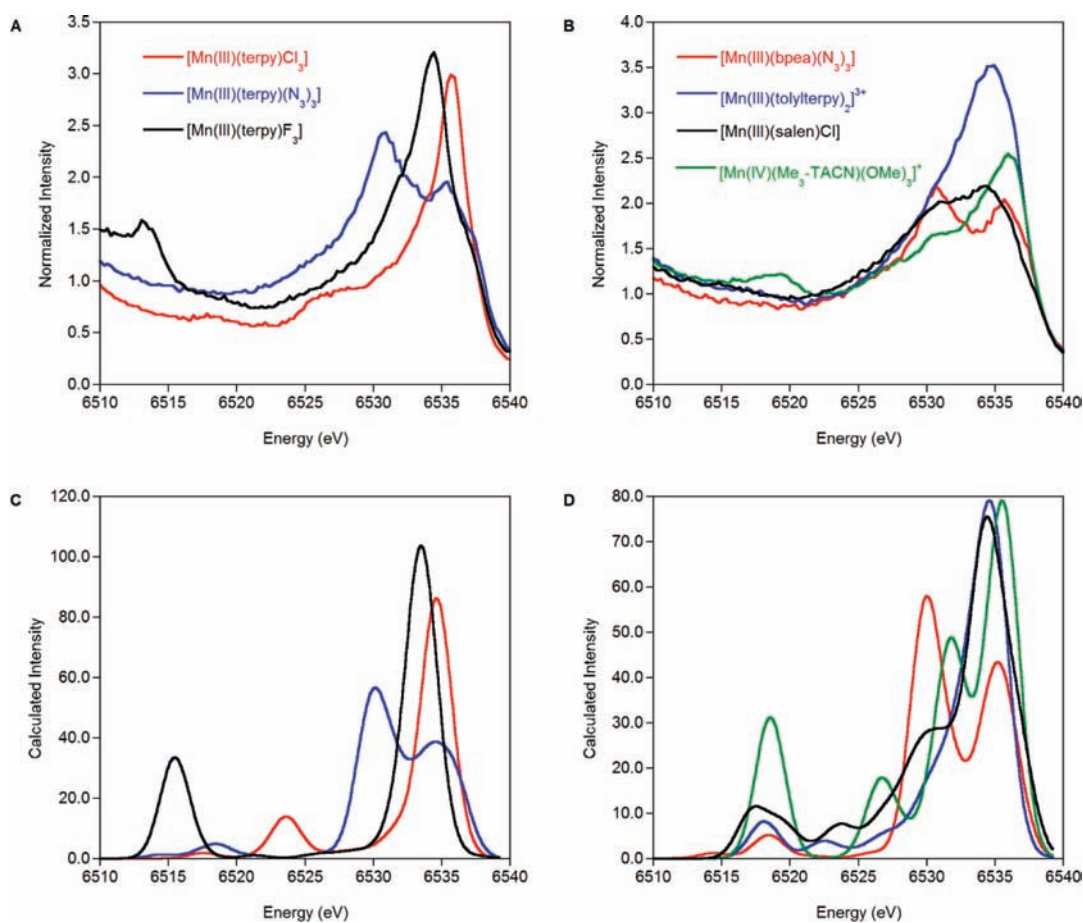
Figure 4. (A and B) Experimental valence to core region for Mn(III) and Mn(IV) complexes. (C and D) Corresponding calculated spectra. A constant shift of 59.2 eV and a 2.5 eV broadening have been applied to all calculated spectra.

although we are perfectly aware that experimentally only the many particle wave functions and states are being probed.

Figure 5 shows the calculated spectrum of $[Mn(III)(terpy)-Cl_3]$ as well as representative MOs that predominately contribute to each feature. The most intense peak at ~6535 eV (Figure 5, feature C) arises from MOs that are primarily composed of Cl-p character, with smaller contributions from C-p and N-p oribtals. A very weak shoulder at ~6539 eV (Figure 5, feature D) corresponds to transitions from the manganese 3d-based t_{2g} set of orbitals, which gains intensity due to ~0.2% Mn p mixing. The lower energy satellite feature at ~6525 eV (Figure 5, feature B) corresponds to transitions from MOs that are dominantly Cl-3s character, while the less intense satellite feature at ~6518 eV (Figure 5, feature A) corresponds to transitions from orbitals that are primarily composed of N-s and C-s character. The most intense features arise from 5—7% Mn-np character mixed into each of the MOs. It should be noted that the satellite feature at ~6525 eV is approximately one-half as intense as the analogous satellite feature in $[Mn(III)(terpy)F_3]$. This is likely due to the differences in the average Mn—Cl and Mn—F bond lengths (2.28 and 1.83 Å, respectively). As discussed previously in the case of iron complexes,[29] the shorter bond length in $[Mn(III)(terpy)F_3]$ increases the amount of Mn-p character that is mixed into the MOs associated with the satellite feature, and this increase in Mn-p mixing raises the intensity of the observed feature.

$[Mn(III)(terpy)(N_3)_3]$. Figure 6 shows the calculated spectrum of $[Mn(III)(terpy)(N_3)_3]$ together with representative MOs

that dominantly contribute to the observed features. Analogous to $[Mn(III)(terpy)Cl_3]$, the valence to core spectrum is composed of transitions from predominantly ligand p orbitals, with 1—7% Mn-p character, thus providing a viable intensity mechanism. The most intense feature at a lower energy of ~6530 eV (Figure 6, feature C) arises from transitions that are predominantly azide N-p and N-s based (48.1% N-p, 19.5% N-s). The orbitals from which these particular transitions originate are primarily metal azide sigma-bonding orbitals with two nodal planes. The lower intensity cluster of transitions between ~6530 and 6531 eV also corresponds to sigma-bonding orbitals; however, the orbitals in this region contain four nodal planes as opposed to two, and thus, the emission transitions occur at slightly higher energies. Regardless of the number of nodal planes, these transitions from metal azide p—sigma-bonding orbitals occur at lower energies than the analogous chlorine p orbitals that form sigma bonds with the metal in $[Mn(III)(terpy)Cl_3]$. This shift to lower energy is a reflection of the difference in the Cl-3p and N-2p ionization energies.

The intense higher energy feature at ~6535 eV (Figure 6, feature D) corresponds to transitions from orbitals that are a mixture of azide N-p and terpy N-p and C-p, with the most intense transition resulting from dominantly terpy N-p and C-p sigma-bonding molecular orbitals. The transitions between ~6535 and 6536 eV result from azide π orbitals interacting with the metal. A lower energy satellite feature at ~6520 eV (Figure 6, feature B) corresponds to transitions from azide N-s and N-p
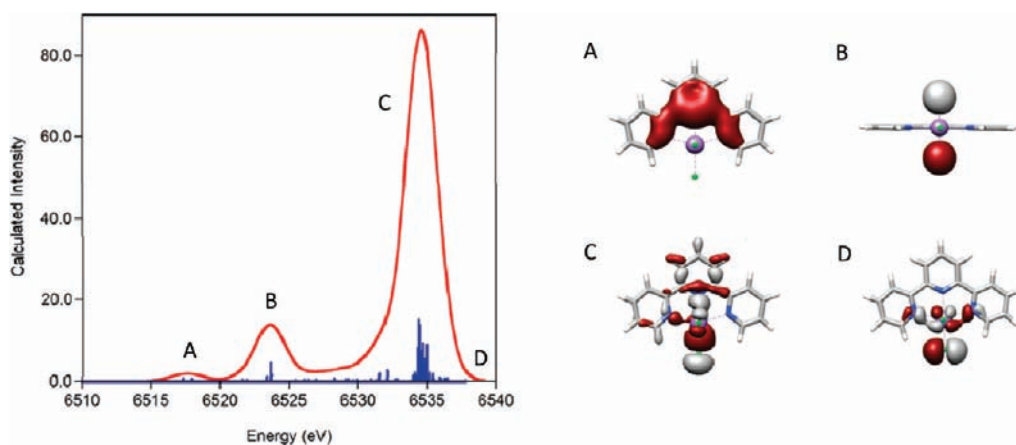
Figure 5. Calculated valence to core spectrum of $[Mn(III)(terpy)Cl_3]$ (left), and predominant molecular orbitals that contribute to the observed transitions (right).
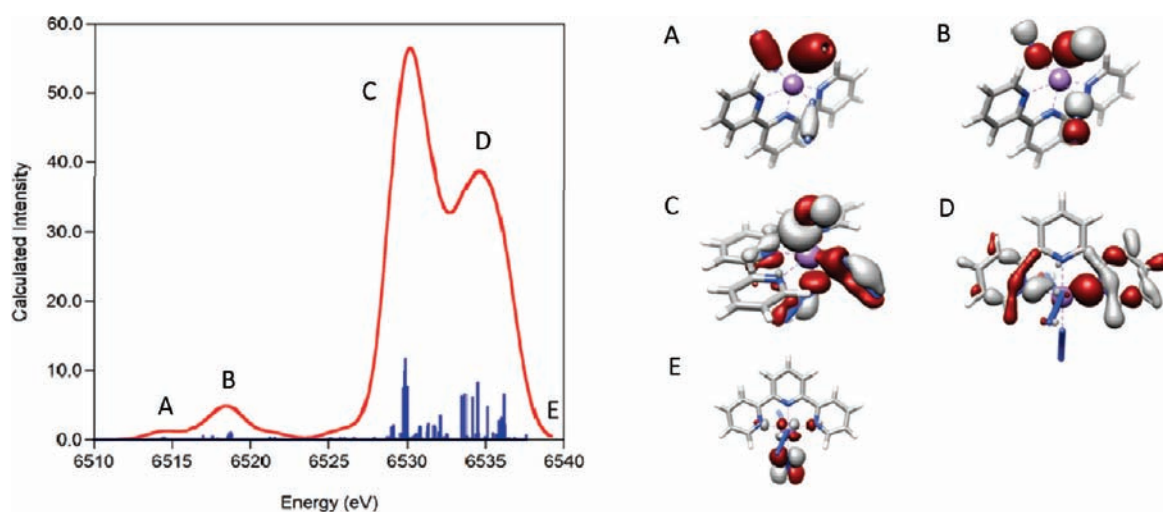

Figure 6. Calculated valence to core spectrum of $[Mn(III)(terpy)(N_3)_3]$ (left), and predominant molecular orbitals that contribute to the observed transitions (right).

orbitals, with one nodal plane within the azide. This feature is shifted by ∼5 eV relative to the most intense satellite feature in $[Mn(III)(terpy)Cl_3]$ and reflects the difference in the Cl-3s and N-2s ionization energies. A lower intensity satellite feature at ∼6515 eV (Figure 6, feature A) corresponds to transitions from azide N-s orbitals with no nodal planes within the azide. The feature at ∼6518 eV in $[Mn(III)(terpy)Cl_3]$ that corresponds to transitions from terpy N-s and C-s is also present in $[Mn(III)-(terpy)(N_3)_3]$, but it cannot be resolved at ∼2.5 eV broadening. As in $[Mn(III)(terpy)Cl_3]$, a very weak shoulder corresponding to transitions from the t_{2g} set of orbitals occurs at ∼6538 eV (Figure 6, feature E). None of the intense transitions are associated with MOs that contain a significant amount of d character. This observation once more supports the dominantly dipole-allowed nature of these transitions.

As the valence to core XES spectra reflect ligand orbitals that are filled in the electronic ground state, the question arises as to whether or not the spectra could help to determine a 10Dq parameter (i.e., via the energy splitting between the dominantly ligand σ-bonding and π-bonding MOs). However, our results show that the intensity is dominantly associated with the

transitions involving MOs that are σ-bonding between the metal and the ligands. Hence, the transitions involving π-bonding orbitals are difficult to identify. In addition, the little intensity that can be attributed to those transitions is often not completely separable from the σ-based intensity.[58]

Hypothetical Molecule Calculations. As noted above, the areas of the experimental valence to core spectra increase significantly (by a factor of ∼1.6) upon oxidation of Mn(II) to Mn(III). In contrast, upon going from a high-spin Fe(II) complex to a high-spin Fe(III) complex only a modest (∼1.1) increase in intensity is observed.[29] These effects are reproduced by the calculations and may offer insight into the physical origin of this differing behavior between the two metals. To this end, a series of calculations was performed on hypothetical molecules involving Mn and Fe in various oxidation states. Figure 7A and 7B shows the calculated spectra for high-spin $[M(II)Cl_6]^{4-}$, $[M(III)Cl_6]^{3-}$, and $[M(IV)Cl_6]^{2-}$ (M = Mn, Fe). A table of bond lengths in provided in the Supporting Information (Table S1).

For the $[MnCl_6]^n$ series there is a shift of all discernible spectral features to higher energy upon oxidation of Mn(II) to
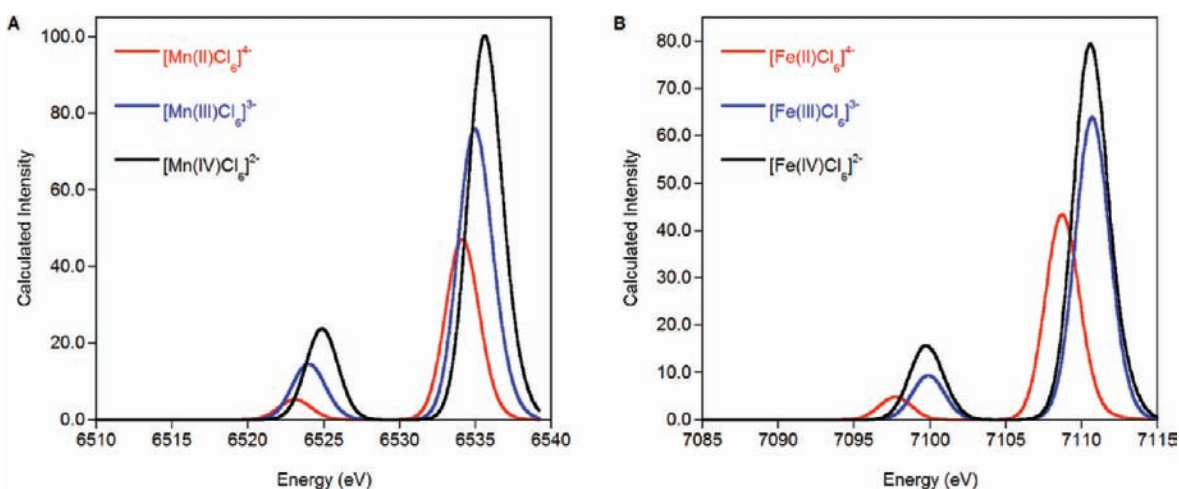
Figure 7. (A) Calculated valence to core spectra for high-spin $[Mn(II)Cl_6]^{4-}$, $[Mn(III)Cl_6]^{3-}$, and $[Mn(IV)Cl_6]^{2-}$. (B) Calculated valence to core spectra for high-spin $[Fe(II)Cl_6]^{4-}$, $[Fe(III)Cl_6]^{3-}$, and $[Fe(IV)Cl_6]^{2-}$. All calculated spectra have been energy shifted to match appropriate experimental values.

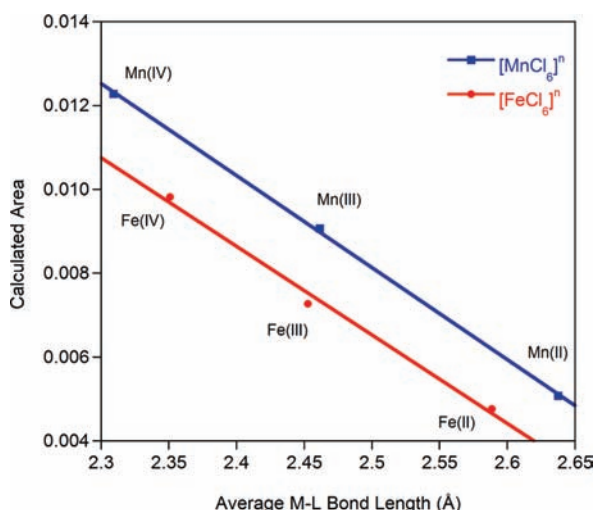**Figure 8.** Calculated area vs average bond length for the $[MnCl_6]^n$ series (blue squares) and for the $[FeCl_6]^n$ series (red circles). The fit for the $[MnCl_6]^n$ series gives a slope of -0.022, and the fit for the $[FeCl_6]^n$ series gives a slope of -0.021.

Mn(III) (by $\sim$0.8 eV) and also upon subsequent oxidation of Mn(III) to Mn(IV). For the $[FeCl_6]^n$ series there is also a shift to higher energy when going from Fe(II) to Fe(III) (by $\sim$2 eV), but there is essentially no change when Fe(III) is oxidized to Fe(IV). This supports the experimental observations and suggests that there are competing Z_{eff} and spin state effects that contribute to the calculated valence to core energies.

Figure 8 shows the relationship between the calculated areas and the calculated bond distances for both series. The relationship is manifestly linear (blue fit line = Mn, red fit line = Fe). We note that previous studies on iron required an exponential fit for a similar series;[29] however, for the shorter range of distances presented here, both linear and exponential fits are equally good.

The calculated areas of the $[MnCl_6]^n$ complexes are on average $\sim$1.2 times larger than the corresponding $[FeCl_6]^n$ complexes of the same metal oxidation state. For both series, the average bond length decreases as oxidation state increases, as

expected; however, the calculated intensity is always higher at Mn even given the same metal—ligand bond length. We note that even if the differences in atomic radii are taken into account,[59] the calculated intensities for Mn are still higher than for Fe (see Figure S2, Supporting Information), though the magnitude of the effect decreases to a factor of $\sim$1.1.

In order to investigate this effect systematically and eliminate all secondary factors that could contribute to the observations, we carried out calculations on the hypothetical molecule $[M(H_2O)_5Cl]^{n+}$, $S = 5/2$ where for M = Fe $n = 2+$ and for M = Mn $n = 1+$. A common idealized geometry was used in which the M—Cl bond is 2.25 Å, the M—OH$_2$ is 2.15 Å long, and all angles are perfectly octahedral.

In order to understand the intensity differences in more detail, we analyzed the composition of the donor orbitals and the intensity contributions for two of the more intense transitions in the two test molecules. Mathematically, the transition dipole moment between a core-1s orbital $\psi_C = \varphi_{M_{1s}}$ and valence orbital $\psi_V = \sum_{\mu A} c_{\mu V} \varphi_\mu^A$ is given by

$$\langle \psi_V | \mathbf{r} | \psi_C \rangle = \sum_{\mu_A} c_{\mu V} \langle \varphi_\mu^A | \mathbf{r} | \varphi_{M_{1s}} \rangle$$

Here, φ_μ^A is the μth basis function centered on Atom A and the $c_{\mu V}$ are the molecular orbital coefficients of the valence orbital. Without compromising generality the origin of the coordinate system can be made to coincide with the metal center. The relevant part of the transition moment is the one that contains metal p character. Thus, one can decompose the transition moment into a local and a nonlocal part. For convenience, a transition polarized along the z axis is considered. However, the arguments hold for arbitrarily polarized transitions.

$$\langle \psi_V | z_M | \psi_C \rangle = \underbrace{c_{M_p}^M \langle \varphi_p^M | z_M | \varphi_{M_{1s}}^B \rangle}_{local} + \underbrace{\sum_{\mu_A (A \neq M)} c_{\mu V} \langle \varphi_\mu^A | z_M | \varphi_{M_{1s}} \rangle}_{non-local}$$

Here, z_M is the z coordinate position operator measured relative to the metal center. One does, of course, expect the local part to strongly dominate. More importantly, however, the local part

8406

dx.doi.org/10.1021/ic200970t |*Inorg. Chem.* 2011, 50, 8397–8409

Table 3. Analysis of the Intensity Mechanism for Two XES Transitons in the 3s (top) and 3p (bottom) Region of the XES Spectra of $[Mn(H_2O)_5Cl]^{1+}$ and $[Fe(H_2O)_5Cl]^{2+}$ [a]

	%M	%Cl	%L	%M_p	OVL	D^2	local	nonlocal	$\langle z_M \rangle_{1s,p}$ ($\times 10^6$)
Cl 3s-donor MO									
Fe	18.1	81.1	0.9	0.18	0.05	316.5	311.7	4.1	7332.3
Mn	19.2	79.6	1.2	0.31	0.09	383.6	376.4	7.2	6702.5
Cl 3p-donor MO									
Fe	23.6	72.7	3.8	1.08	0.11	672.8	660.7	12.1	6333.6
Mn	15.6	82.2	2.3	0.94	0.11	731.7	7161.1	15.6	7346.1

[a] Listed are the percentage metal character (%M), Cl character (%Cl), and remaining ligands (%L) in the XES donor orbitals, the gross metal p character (%M_p), the overlap charge between the metal and all ligands (OVL), the total transition dipole moment squared (D^2, in au^2), the local and nonlocal contributions to the transition dipole moment, and the local radial expectation value of the position operator renormalized to unit metal p character.

contains two contributions: the metal p character mixed into the valence MO (measured by $(c_{M_p}^M)^2$) and the local transition dipole moment $\langle \varphi_p^M | z_M | \varphi_{M_{1s}}^B \rangle$. From atomic calculations we found that the local transition dipole moments for manganese and iron are very similar (e.g., 0.00776 au for Mn^{2+}, 0.00755 au for Fe^{2+}, and 0.00765 au for Fe^{3+}). Thus, the differences on the order of 1−2% cannot explain the differences in the observed intensities, which is an order of magnitude larger. However, the radial functions distort in the molecular environment as a consequence of chemical bonding. Hence, the atomic transition dipole moment values will be modified. In order to understand the dominating factors in more detail, the two most intense transitions in the 3s and 3p regions of the of the XES spectra for $[M(H_2O)_5Cl]^{n+}$ are analyzed in Table 3.

First, the data in Table 3 demonstrates that the local contributions indeed dominate the transition dipole moment, however, perhaps not as strongly as anticipated. The nonlocal terms account for about 1−3% of the total transition dipole. However, their values are not drastically different for the two metals, and hence, they warrant no further discussion. In the Cl 3s region of the XES spectra, it seems clear that the main reason for the manganese contribution to the transition dipole moment is the larger amount of metal p character mixed into the valence MO. The local transition dipole moment is actually considerably reduced for manganese from its atomic value. Yet, the almost factor of 2 higher metal p character more than in the atomic case compensates for this.

In the Cl 3p region of the XES spectrum the situation is reversed. Here, the metal p character is rather similar for both metals but the local manganese transition dipole moment is much higher than in the iron case.

In both cases, the net result is that the intensity in manganese spectra is higher, which is in agreement with the experimental observations. The reasons, however, are fairly subtle and related to both the distortion of the metal p orbitals in the molecular environment and the amount of p character mixed into the valence orbitals. The differences presumably arise from a subtle interplay of factors. It is evident from our previous work that it is both metal 3p and 4p character that contributes to the intensity in the crossover region of the XES spectra. Obviously, the amount of mixing between the 3p and the 4p set of metal orbitals with the ligand orbitals depends on their energetic position relative to the ligand orbitals. This position in turn depends on the effective nuclear charge of the metal ion and varies with oxidation and spin state. However, the 3p and 4p sets behave differently. In the 3p set, the p character in the valence

orbitals is of antibonding nature, which will tend to expand the radial wave function, which in turn will increase the radial expectation value. For the 4p set, the mixed-in p character will be of bonding nature, which will tend to contract the radial wave function and decrease the radial expectation value. Both types of behavior are found in Table 3, thus underlining how complex the problem is. In addition, the metal character is very small and only amounts to a fraction of a percent (i.e., *two* orders of magnitude less than the total metal character in these orbitals). Obviously, capturing such small effects accurately places stringent requirements on the calculations. However, the calculations appear to reproduce the trends in the experimental data largely correctly, which implies that despite the fact that the effect is very small the leading physically relevant contributions to the intensity are captured correctly.

■ CONCLUSIONS

A systematic experimental and computational study of Mn Kβ XES spectra for a series of high-spin mononuclear manganese complexes has been presented. The study has focused on the valence to core region of the XES spectra. This region shows a pronounced sensitivity to the chemical environment and reacts to differences in oxidation state, spin state, and ligand identity.

The generally good agreement between experimental and calculated spectra has allowed for a more detailed investigation of the orbital contributions to the experimental valence to core spectra. As expected, the spectra are dominated by dipole-allowed Mn np to 1s transitions. The energy shifts observed in this region are a result of both the effective nuclear charge at the manganese and the spin state effects. They have been shown to have opposing effects on the resulting spectra for the most common oxidation states of manganese (+2 to +4), thus resulting in smaller overall energetic differences than have previously been observed for Fe valence to core XES spectra.[29]

On the basis of our results, the valence to core area appears to be a reliable indicator of Mn oxidation state: as the oxidation state increases, the area also increases significantly. This is in contrast to what has been observed for Fe, where the valence to core area did not change significantly upon oxidation of Fe complexes of the same spin state.[29] These differences between the trends for Mn and Fe areas are, in part, a result of the more pronounced bond length changes for Mn. They arise due to more significant Jahn−Teller effects in Mn complexes compared to Fe complexes: in Mn complexes the Jahn−Teller active configuration occurs at Mn(III), while in Fe it is Fe(II), which has much weaker

metal—ligand bond distances. The differences between Mn and Fe are also partially due to differences in the distortions of the metal p orbitals in a molecular environment as well as differences in the amount of p character mixed into the valence orbitals.

In addition to spin and oxidation state, the Mn valence to core region is also sensitive to ligand identity, showing ligand np and ns contributions, similar to what was seen previously in Fe complexes. Specifically for Mn, the valence to core spectra may allow for separation of different ligand contributions within heteroleptic environments, as seen in the dramatic differences between the spectra of $[Mn(III)(tolylterpy)_2]^{3+}$ and $[Mn(III)(terpy)(N_3)_3]$, for example. This sensitivity to ligand environment, along with the strong correlation between experiment and theory, suggests that the valence to core region of the XES spectra may be a useful predictive tool for examining Mn active sites in biological systems. The calibration study presented here forms the basis for future quantitative studies of the XES spectra in complex ligand environments, including the Mn_4Ca cluster in the active site of photosystem II.[11,60,61]

■ ASSOCIATED CONTENT

Ⓢ Supporting Information. This material is available free of charge via the Internet at http://pubs.acs.org.

■ AUTHOR INFORMATION

Corresponding Author
*E-mail: serena.debeer@cornell.edu.

Present Addresses
○Stanford Synchrotron Radiation Lightsource, SLAC National Accelerator Laboratory, Menlo Park, CA 94025, United States.

■ ACKNOWLEDGMENT

■ REFERENCES

(1) Abreu, I. A.; Cabelli, D. E. *BBA-Proteins Proteomics* **2010**, *1804*, 263.

(2) Abreu, I. A.; Rodriguez, J. A.; Cabelli, D. E. *J. Phys. Chem. B* **2005**, *109*, 24502.

(3) Fridovich, I. *Annu. Rev. Biochem.* **1995**, *64*, 97.

(4) Pecoraro, V. L.; Hsieh, W.-Y. In *Manganese and Its Role in Biological Processes*; Sigel, A., Sigel, H., Eds.; Marcel Dekker Inc: New York, 2000; Vol. 37, pp 429—504.

(5) Vrettos, J. S.; Brudvig, G. W. *Philos. Trans. R. Soc. London, Ser. B* **2002**, *357*, 1395.

(6) Fu, B.; Yu, H. C.; Huang, J. W.; Zhao, P.; Liu, J.; Ji, L. N. *J. Mol. Catal. A:Chem.* **2009**, *298*, 74.

(7) Gupta, K. C.; Sutar, A. K.; Lin, C. C. *Coord. Chem. Rev.* **2009**, *253*, 1926.

(8) McLain, J. L.; Lee, J.; Groves, J. T. In *Biomimetic Oxidation Catalyzed by Transition Metal Complexes*; Meunier, B., Ed.; Imperial College Press: London, 2000; pp 91—169.

(9) Palucki, M.; Finney, N. S.; Pospisil, P. J.; Güler, M. L.; Ishida, T.; Jacobsen, E. N. *J. Am. Chem. Soc.* **1999**, *120*, 948.

(10) Tabares, L. C.; Gatjens, J.; Un, S. *BBA-Proteins Proteomics* **2010**, *1804*, 308.

(11) Messinger, J.; Robblee, J. H.; Bergmann, U.; Fernandez, C.; Glatzel, P.; Visser, H.; Cinco, R. M.; McFarlane, K. L.; Bellacchio, E.; Pizarro, S. A.; Cramer, S. P.; Sauer, K.; Klein, M. P.; Yachandra, V. K. *J. Am. Chem. Soc.* **2001**, *123*, 7804.

(12) Su, J. H.; Lubitz, W.; Messinger, J. *J. Am. Chem. Soc.* **2008**, *130*, 786.

(13) Su, J. H.; Messinger, J. *Appl. Magn. Reson.* **2010**, *37*, 123.

(14) de Groot, F. M. F. *Chem. Rev.* **2001**, *101*, 1779.

(15) Mukoyama, T. *Spectrochim. Acta, Part B: Atom. Spectros.* **2004**, *59*, 1107.

(16) Penner-Hahn, J. E. *Coord. Chem. Rev.* **2005**, *249*, 161.

(17) Qian, Q.; Tyson, T. A.; Kao, C. C.; Croft, M.; Cheong, S. W.; Popov, G.; Greenblatt, M. *Phys. Rev. B* **2001**, *64*, 024430.

(18) Strange, R. W.; Ellis, M.; Hasnain, S. S. *Coord. Chem. Rev.* **2005**, *249*, 197.

(19) Yano, J.; Kern, J.; Irrgang, K. D.; Latimer, M. J.; Bergmann, U.; Glatzel, P.; Pushkar, Y.; Biesiadka, J.; Loll, B.; Sauer, K.; Messinger, J.; Zouni, A.; Yachandra, V. K. *Proc. Natl. Acad. Sci. U.S.A.* **2005**, *102*, 12047.

(20) Yano, J.; Kern, J.; Sauer, K.; Latimer, M. J.; Pushkar, Y.; Biesiadka, J.; Loll, B.; Saenger, W.; Messinger, J.; Zouni, A.; Yachandra, V. K. *Science* **2006**, *314*, 821.

(21) Yano, J.; Yachandra, V. K. *Inorg. Chem.* **2008**, *47*, 1711.

(22) Bergmann, U.; Glatzel, P.; Robblee, J. H.; Messinger, J.; Fernandez, C.; Cinco, R.; Visser, H.; McFarlane, K.; Bellacchio, E.; Pizarro, S.; Sauer, K.; Yachandra, V. K.; Klein, M. P.; Cox, B. L.; Nealson, K. H.; Cramer, S. P. *J. Synchrotron Radiat.* **2001**, *8*, 199.

(23) Glatzel, P.; Bergmann, U. *Coord. Chem. Rev.* **2005**, *249*, 65.

(24) Glatzel, P.; Bergmann, U.; deGroot, F. M. F.; Cramer, S. P. *Phys. Rev. B* **2001**, *64*, 045109.

(25) Peng, G.; deGroot, F. M. F.; Hamalainen, K.; Moore, J. A.; Wang, X.; Grush, M. M.; Hastings, J. B.; Siddons, D. P.; Armstrong, W. H.; Mullins, O. C.; Cramer, S. P. *J. Am. Chem. Soc.* **1994**, *116*, 2914.

(26) Visser, H.; Anxolabéhère-Mallart, E.; Bergmann, U.; Glatzel, P.; Robblee, J. H.; Cramer, S. P.; Girerd, J.-J.; Sauer, K.; Klein, M. P.; Yachandra, V. K. *J. Am. Chem. Soc.* **2001**, *123*, 7031.

(27) Bergmann, U.; Bendix, J.; Glatzel, P.; Gray, H. B.; Cramer, S. P. *J. Chem. Phys.* **2002**, *116*, 2011.

(28) Bergmann, U.; Horne, C. R.; Collins, T. J.; Workman, J. M.; Cramer, S. P. *Chem. Phys. Lett.* **1999**, *302*, 119.

(29) Lee, N.; Petrenko, T.; Bergmann, U.; Neese, F.; DeBeer, S. *J. Am. Chem. Soc.* **2010**, *132*, 9715.

(30) Smolentsev, G.; Soldatov, A. V.; Messinger, J.; Merz, K.; Weyhermüller, T.; Bergmann, U.; Pushkar, Y.; Yano, J.; Yachandra, V. K.; Glatzel, P. *J. Am. Chem. Soc.* **2009**, *131*, 13161.

(31) Pushkar, Y.; Long, X.; Glatzel, P.; Brudvig, G. W.; Dismukes, G. C.; Collins, T. J.; Yachandra, V. K.; Yano, J.; Bergmann, U. *Angew. Chem., Int. Ed.* **2010**, *49*, 800.

(32) Baffert, C.; Romero, I.; Pécaut, J.; Llobet, A; Deronzier, A.; Collomb, M.-N. *Inorg. Chim. Acta* **2004**, *357*, 3430.

(33) Duboc, C.; Collomb, M. N. *Chem. Commun.* **2009**, *19*, 2715.

(34) Duboc, C.; Collomb, M. N.; Pécaut, J.; Deronzier, A.; Neese, F. *Chem.—Eur. J.* **2008**, *14*, 6498.

(35) Limburg, J.; Vrettos, J. S.; Crabtree, R. H.; Brudvig, G. W.; Paula, J. C. d.; Hassan, A.; Barra, A.-L; Duboc-Toia, C.; Collomb, M.-N. *Inorg. Chem.* **2001**, *40*, 1698.

(36) Mantel, C.; Baffert, C.; Romero, I.; Deronzier, A.; Pécaut, J.; Collomb, M. N.; Duboc, C. *Inorg. Chem.* **2004**, *43*, 6455.

(37) Mantel, C.; Chen, H. Y.; Crabtree, R. H.; Brudvig, G. W.; Pécaut, J.; Collomb, M. N.; Duboc, C. *Chem. Phys. Chem.* **2005**, *6*, 541.

(38) Mantel, C.; Hassan, A. K.; Pécaut, J.; Deronzier, A.; Collomb, M. N.; Duboc-Toia, C. *J. Am. Chem. Soc.* **2003**, *125*, 12337.

(39) Mantel, C.; Philouze, C.; Collomb, M. N.; Duboc, C. *Eur. J. Inorg. Chem.* **2004**, *19*, 3880.

(40) Quee-Smith, V. C.; DelPizzo, L.; Jureller, S. H.; Kerschner, J. L.; Hage, R. *Inorg. Chem.* **1996**, *35*, 6461.

(41) Rich, J.; Castillo, C. E.; Romero, I.; Rodríguez, M.; Duboc, C.; Collomb, M. N. *Eur. J. Inorg. Chem.* **2010**, *23*, 3658.

(42) Romain, S.; Baffert, C.; Duboc, C.; Lepretre, J. C.; Deronzier, A.; Collomb, M. N. *Inorg. Chem.* **2009**, *48*, 3125.

(43) Romain, S.; Duboc, C.; Neese, F.; Rivière, E.; Hanton, L. R.; Blackman, A. G.; Philouze, C.; Leprêtre, J.-C.; Deronzier, A.; Collomb, M.-N. *Chem.—Eur. J.* **2009**, *15*, 980.

(44) Solé, V. A.; Papillon, E.; Cotte, M.; Walter, P.; Susini, J. *Spectrochim. Acta, Part B* **2007**, *62*, 63.

(45) George, G. N. *EXAFSPAK, SSRL, SLAC*; Stanford University: Stanford, CA, 2000.

(46) Becke, A. D. *Phys. Rev. A* **1988**, *38*, 3098.

(47) Perdew, J. P. *Phys. Rev. B* **1986**, *33*, 8822.

(48) Lenthe, E. v.; Avoird, A. v. d.; Wormer, P. E. S. *J. Chem. Phys.* **1998**, *108*, 4783.

(49) van Wüllen, C. *J. Chem. Phys.* **1998**, *109*, 392.

(50) Pantazis, D. A.; Chen, X. Y.; Landis, C. R.; Neese, F. *J. Chem. Theory Comput.* **2008**, *4*, 908.

(51) Klamt, A.; Schüürmann, G. *J. Chem. Soc., Perkin Trans. 2* **1993**, *5*, 799.

(52) Hess, B. A.; Marian, C. M.; Wahlgren, U.; Gropen, O. *Chem. Phys. Lett.* **1996**, *251* (5−6), 365–371.

(53) Herrero-Martin, J.; Mirone, A.; Fernandez-Rodriguez, J.; Glatzel, P.; Garcia, J.; Blasco, J.; Geck, J. *Phys. Rev. B* **2010**, *82*, 075112.

(54) Neese, F. *ORCA-an ab initio,density functional and semiempirical program package*, Version 2.7; University of Bonn: Bonn, Germany, 2010.

(55) de Groot, F. M. F. *Coord. Chem. Rev.* **2005**, *249*, 31.

(56) DeBeer George, S.; Petrenko, T.; Neese, F. *J. Phys. Chem. A* **2008**, *112*, 12936.

(57) DeBeer George, S.; Petrenko, T.; Neese, F. *Inorg. Chim. Acta* **2008**, *361*, 965.

(58) Pollock, C. J.; DeBeer, S. *J. Am. Chem. Soc.* **2011**, *133*, 5594.

(59) Shannon, R. D. *Acta Crystallogr., Sect. A* **1976**, *32*, 751.

(60) Bergmann, U.; Grush, M. M.; Horne, C. R.; DeMarois, P.; Penner-Hahn, J. E.; Yocum, C. F.; Wright, D. W.; Dubé, C. E.; Armstrong, W. H.; Christou, G.; Eppley, H. J.; Cramer, S. P. *J. Phys. Chem. B* **1998**, *102*, 8350.

(61) Glatzel, P.; Bergmann, U.; Yano, J.; Visser, H.; Robblee, J. H.; Gu, W. W.; deGroot, F. M. F.; Christou, G.; Pecoraro, V. L.; Cramer, S. P.; Yachandra, V. K. *J. Am. Chem. Soc.* **2004**, *126*, 9946.

■ NOTE ADDED AFTER ASAP PUBLICATION

This paper was published on the Web on August 1, 2011. Minor text corrections were added and the corrected version was reposted on August 3, 2011.

8409

dx.doi.org/10.1021/ic200970t |*Inorg. Chem.* 2011, 50, 8397–8409